

Multi-Agent Meta-Advisor for UAV Fleet Trajectory Design in Vehicular Networks

Leonardo Spampinato, Lorenzo Mario Amorosa, Enrico Testi, Chiara Buratti, Riccardo Marini

Abstract—Future vehicular networks require continuous connectivity to serve highly mobile users in urban environments. To mitigate the coverage limitations of fixed terrestrial macro base stations (MBS) under non line-of-sight (NLoS) conditions, fleets of unmanned aerial base stations (UABSs) can be deployed as aerial base stations, dynamically repositioning to track vehicular users and traffic hotspots in coordination with the terrestrial network. This paper addresses cooperative multi-agent trajectory design under different service areas and takeoff configurations, where rapid and safe adaptation across scenarios is essential. We formulate the problem as a multi-task decentralized partially observable Markov decision process and solve it using centralized training and decentralized execution with double dueling deep Q-network (3DQN), enabling online training for real-world deployments. However, efficient exploration remains a bottleneck, with conventional strategies like ϵ -greedy requiring careful tuning. To overcome this, we propose the multi-agent meta-advisor with advisor override (MAMO). This framework guides agent exploration through a meta-policy learned jointly across tasks. It uses a dynamic override mechanism that allows agents to reject misaligned guidance when the advisor fails to generalize to a specific scenario. Simulation results across three realistic urban scenarios and multiple takeoff configurations show that MAMO achieves faster convergence and higher returns than tuned ϵ -greedy baselines, outperforming both an advisor-only ablation and a single generalized policy. Finally, we demonstrate that the learned UABS fleet significantly improves network performance compared to deployments without aerial support.

Index Terms—Meta learning, Vehicular networks, UAVs, Multi agent systems, Trajectory design

I. INTRODUCTION

The evolution of 6G systems envisions support for vehicle-to-everything (V2X) communications, which demand stringent network requirements for safety-critical applications [1]–[4]. However, the intrinsic high mobility of ground user equipments (GUEs), coupled with spatio-temporal fluctuations in traffic density, presents unique obstacles to efficient network service [5]–[7]. In such dynamic scenarios, existing fixed macro base station (MBS) deployments often fail to provide continuous connectivity. Signal paths are frequently obstructed by buildings, resulting in severe non line-of-sight (NLoS)

Copyright (c) 2025 IEEE. Personal use of this material is permitted. However, permission to use this material for any other purposes must be obtained from the IEEE by sending a request to pubs-permissions@ieee.org (*Corresponding author: Leonardo Spampinato*).

Leonardo Spampinato, Lorenzo Mario Amorosa, Enrico Testi, Chiara Buratti, and Riccardo Marini are with the National Laboratory of Wireless Communications of CNIT (Wilab, CNIT), Italy. (e-mail: leonardo.spampinato@unibo.it; lorenzomario.amorosa@unibo.it; enrico.testi@unibo.it; c.buratti@unibo.it; riccardo.marini@wilab.cnit.it).

Leonardo Spampinato, Lorenzo Mario Amorosa, Enrico Testi, and Chiara Buratti are also with the Department of Electrical, Energy, and Information Engineering, University of Bologna, Italy.

conditions and coverage gaps that degrade service quality [8]–[11]. To mitigate these issues, the use of unmanned aerial base stations (UABSs) has emerged as a promising solution. By acting as aerial integrated access and backhaul relays, UABSs can provide on-demand capacity boost [12]–[14]. The effectiveness of a UABS fleet is determined by its dynamic positioning strategy. Leveraging their unmatched mobility, they can continuously adjust their trajectories to track vehicular users and anticipate service demand hotspots, both in time and space, while coordinating with the underlying terrestrial MBS for backhauling and interference management through joint terrestrial-aerial radio resource management (RRM). Thus, the problem of fleet trajectory design becomes critical. The use of the multi-agent deep reinforcement learning (MADRL) algorithm is envisioned to enable the fleet to learn an adaptive trajectory planning model, allowing UABSs to autonomously cooperate to guarantee strict V2X quality of experience (QoE) requirements.

However, in real-world deployment, the fleet may be required to serve distinct service areas, each with a given road layout and traffic density, or be dispatched from diverse takeoff positions within the same area. A robust design solution must possess the capability to adapt its operational behavior across these diverse scenarios without requiring a computationally expensive redesign each time a new operational scenario is introduced. Achieving such rapid adaptation poses a significant challenge, particularly for state-of-the-art MADRL approaches. These methods typically require extensive retraining whenever deployment conditions change, relying on inefficient random exploration strategies [15]–[17]. In the context of a UABS-assisted V2X network, the resulting transient performance degradation caused by this retraining is prohibitive. Consequently, developing mechanisms for rapid and safe adaptation across multiple deployment scenarios is fundamental for real-world viability. To address these challenges, and building upon our previous work in [18], we propose the multi-agent meta-advisor with advisor override (MAMO) framework. MAMO introduces a meta-advisor that guides the exploration phase of multi-agent systems. Rather than relying on random exploration strategies, agents receive guidance from a meta-policy that is learned jointly across multiple fleet configurations, providing generalization across the considered set of tasks. By aggregating experience across operation scenarios, the advisor processes agents' local observations to suggest exploration actions that accelerate per-task adaptation. The framework further incorporates a dynamic override mechanism that enables agents to evaluate the advisor's recommendations against their own task-specific policies. By allowing agents

to reject task-mismatched guidance, e.g., when the advisor becomes over-confident toward only a subset of tasks, MAMO ensures rapid adaptation to new environments while remaining robust to unique local conditions that a generalized advisor may fail to capture. Overall, MAMO provides a safer and more efficient learning paradigm, significantly reducing the time-to-proficiency in multi-task adaptation. The main contributions of this paper are summarized as follows:

- we define a multi-task formulation for cooperative UABS fleet trajectory design within a V2X network, accounting for integrated terrestrial-aerial RRM and adaptation requirements across diverse operational environments;
- we introduce a MADRL algorithm utilizing a centralized training decentralized execution (CTDE) architecture that exploits available network links to enable online training capabilities for the fleet, ensuring the system is applicable to real-world deployment scenarios;
- we propose the MAMO exploration framework to drive effective adaptation via enhanced exploration among diverse tasks, directly improving the time-to-proficiency and operational readiness of the trained agents;
- we validate our framework through extensive simulations in realistic urban scenarios, demonstrating significant gains in training efficiency and convergence speed across a wide range of task settings compared to standard approaches.

The remainder of the paper is organized as follows: in Section II, the state-of-the-art on multi-agent exploration strategies is reported; Section III presents the considered system model; Section IV introduces the fleet trajectory design problem formulation and the adopted MADRL system; Section V describes the exploration strategies investigated in our work, and details the proposed MAMO solution; Section VI reports numerical results, and in Section VII, conclusions are drawn.

II. RELATED WORK

The efficacy of MADRL systems training relies on the exploration strategy adopted, especially in high-dimensional and dynamic environments such as UABS fleet trajectory planning [19]–[21]. Conventional approaches, such as ϵ -greedy, can be inefficient or require careful tuning, which is impractical for online learning in deployed networks [22]–[25]. Accordingly, recent MADRL literature has investigated mechanisms to improve exploration efficiency and stability, including intrinsic motivation, meta-learning, role-awareness, and teacher/advisor paradigms. In the following, we review these directions and discuss their limitations in UABS-aided vehicular networks, where learning should be fast, safe, and robust to heterogeneous deployment conditions.

Curiosity-driven exploration is widely used to address sparse rewards by augmenting the learning signal with intrinsic exploration bonuses. In [26], a strangeness-driven mechanism is proposed that promotes exploration of novel joint states, while [27] extends prediction error-based intrinsic rewards to local agent observations, improving exploration under partial observability. However, these approaches require task-specific reward tuning, limiting their applicability in heterogeneous deployments, and auxiliary reward shaping can degrade network

performance during training. In contrast, our approach avoids the need for auxiliary intrinsic reward by delegating exploration to a separate advisor that is meta-trained to generalize across various tasks and promoting cross-task adaptability.

Meta-reinforcement learning and advisor-based exploration aim to transfer knowledge across a task distribution, thus accelerating adaptation. In [28], an external advisor is learned in a meta-markov decision process (MDP), while [29] studies how agents can selectively follow advice based on its trustworthiness for the current task. A key practical limitation is that many advisor approaches rely on separate offline pre-training phases, which may reduce online applicability. In contrast, our advisor is a modular component decoupled from the exploitation policy. It can be trained in parallel with the agents and online, using its own algorithm and hyperparameters. In this work, we implement it as a value-based off-policy learner to exploit experience replay and improve sample-efficiency across tasks.

Other works improve exploration by learning agent roles or estimating agent influence. In [30], ROMA discovers emergent roles that guide exploration, while [31] introduces MAVEN, which leverages latent variables to encourage policy diversity. Similarly, [32] proposes an influence-based mechanism that promotes exploration by rewarding agents with higher team impact. While these approaches enhance decentralized exploration diversity, they often suffer from brittle role assignments or unstable learning under dynamic task distributions. In contrast, our advisor is trained explicitly to handle variability in the environment configuration, like service maps and drone takeoff positions, without relying on latent role discovery or manually shaped influence models.

Some works enhance exploration by augmenting the learning signal through representation learning. In [33], contrastive learning is used to obtain diverse feature encodings, while [34] proposes predictive models to learn informative state abstractions. While often beneficial, these methods typically increase training complexity, requiring auxiliary losses and additional modules, and may require a broad set of solvable tasks to generalize in a reliable way. In comparison, our method maintains simplicity and modularity by leveraging an augmented state representation that includes context features, i.e., simple known task descriptors, thus eliminating the need for learnable auxiliary predictions or models. In summary, most existing approaches rely on (i) modifying reward functions with intrinsic signals, (ii) enforcing structural biases via role definitions, or (iii) increasing complexity through representation learning. While effective in static environments, the computational overhead and rigidity of these methods often limit their utility in scenarios requiring efficient online training. To overcome these limitations without adding structural complexity to the agents themselves, we introduce a multi-agent meta-advisor. This modular component learns a generalized exploration policy across diverse scenarios, enabling multi-task adaptation. Because the advisor is decoupled from the agent's core architecture, it can be trained online with independent hyperparameter tuning, making it ideal for UABS fleet trajectory design, where fast and safe convergence is critical for service continuity.

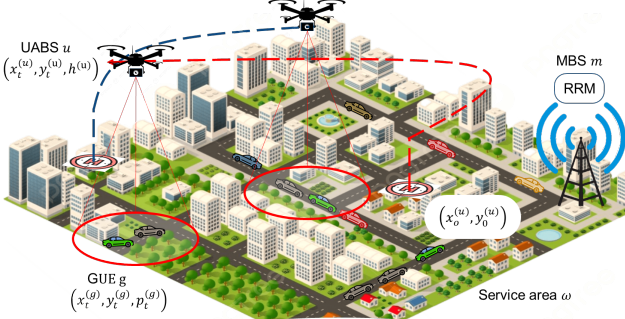


Fig. 1: Representation of the reference scenario.

III. SYSTEM MODEL

A. Reference Scenario

We consider an urban scenario in which a set of GUEs denoted by \mathcal{G} , participates in a V2X application. Each GUE $g \in \mathcal{G}$ periodically generates and uploads data packets to the network within a designated service area $\omega \in \Omega$, where Ω denotes the set of service areas considered. Each area is characterized by a specific street layout map, within which users travel according to a specific road traffic distribution. Cellular coverage within ω is provided by a terrestrial MBS, denoted by m , operating at carrier frequency f_c in millimeter wave (mmWave). The location of the MBS is given by $(x_\omega^{(m)}, y_\omega^{(m)})$, where this notation highlights the MBS dependence on the specific service area $\omega \in \Omega$.

To complement the fixed terrestrial infrastructure and mitigate its limitations in terms of coverage and capacity, a fleet of UABSSs, denoted by the set \mathcal{U} , is deployed in each area. The UABSSs act as aerial base stations, providing additional access opportunities to the GUEs, aiming at enhancing the overall system performance. Each UABSS $u \in \mathcal{U}$ is assumed to move at a flying speed $v^{(u)}$ at a fixed altitude $h^{(u)}$. However, their trajectory is not given a priori. Each UABSS performs a flight mission of duration T which consists of a sequence of discrete timesteps $t = 0, 1, \dots, T$, each of duration Δt . At each time step, the positions of the UABSSs are represented as $(x_t^{(u)}, y_t^{(u)}) \forall u \in \mathcal{U}$. The ordered sequence $\mathbf{P}_t = (x_t^{(u)}, y_t^{(u)} \mid u \in \mathcal{U})$ represents the positions of all UABSSs in the fleet at time step t , with \mathbf{P}_0 denoting their takeoff coordinates.

Each UABSS maintains a wireless backhaul link to the MBS, ensuring continuous connectivity with the terrestrial infrastructure. Through this link, user traffic from GUEs served by UABSSs is relayed to the core network, while operational commands are exchanged to coordinate UABSS behavior. This backhaul connection is essential for seamless integration of UABSSs operations within the network. Since UABSSs operate within the same frequency band as the terrestrial network, their deployment requires no additional spectrum allocation for mobile operators. However, this shared spectrum approach demands careful interference management to maintain network performance. To address this challenge, resource management is centralized at the MBS, which acts as the controller for both terrestrial and aerial network segments. A RRM algorithm running at the MBS dynamically manages user association

and radio resource allocation, determining whether each GUE should connect to the MBS or to a UABSS. The algorithm maximizes the continuity of service of served users, accounting for potential interference.

Within this scenario, our goal is to determine flight mission fleet trajectories $\mathbf{P}_{0:T,\omega} = [\mathbf{P}_0, \mathbf{P}_1, \dots, \mathbf{P}_T]_\omega$ that maximize the overall network performance in coordination with the MBS through joint aerial-terrestrial RRM, for each service area ω and takeoff locations \mathbf{P}_0 considered. A representation of the considered scenario is shown in Fig. 1.

B. Reference Application

Users move within the considered service area $\omega \in \Omega$ based on its street layout and traffic distribution, with their time-varying position denoted as $(x_t^{(g)}, y_t^{(g)})$. Each GUE $g \in \mathcal{G}$ periodically generates cooperative awareness messages (CAMs) messages of fixed size D_g , requesting radio resources for the transmission. This setup corresponds to an extended sensing scenario, where GUEs continuously offload locally gathered sensor data, ranging from telemetry to high-definition video feeds, to the network infrastructure [35].

Within the service area, a GUE g is said to be *covered* by a base station (BS), where a BS is either the MBS or a UABSS, if the corresponding wireless link among the two terminals achieves a signal to interference plus noise ratio (SINR) above a predefined threshold SINR_{th} . We model this using the binary variables $c_t^{(g,m)}$ and $c_t^{(g,u)}$, which are equal to 1 if g is covered by the MBS m or by a UABSS $u \in \mathcal{U}$, respectively. These variables are determined based on the SINR computation detailed in Sec. III-C, and depend primarily on the positions between GUEs, MBS, and UABSSs in the fleet.

Given the network coverage state, which allows to estimate the achievable rates, a centralized RRM algorithm determines the optimal user association and uplink resource scheduling at each time step. To this end, a GUE g is considered *served* at time step t if the RRM algorithm has assigned sufficient resources to upload its data packet, as part of its optimization output process. This is represented by the binary variables $\psi_t^{(g)}$, which equals 1 when g is served and 0 otherwise. We further define $\psi_t^{(g,m)}$ and $\psi_t^{(g,u)}$ to indicate whether it has been served by MBS m or a UABSS $u \in \mathcal{U}$, respectively. A user can be served by at most one BS. Details on the RRM algorithm formulation are reported in Appendix A.

To capture the continuous service requirements typical of vehicular applications, we define a GUE g as *satisfied* if it is served for at least \hat{N}_s time steps within its service window W_g . Each service window W_g comprises N_w time steps and lasts for $T_w = N_w \Delta t$. The QoE requirement \hat{N}_s reflects the time a vehicle may take to maneuver, such as turning at intersections or roundabouts. Example values can be found in [36].

To track the current service continuity status at each time step t , a priority metric $p_t^{(g)}$ is assigned to each GUE g to count the number of times each g has been served in its current service window W_g . In particular, within each service time window W_g (i.e., at time steps $t = 1, \dots, N_w$) $p_t^{(g)}$ varies as

follows:

$$p_t^{(g)} = \begin{cases} 1, & \text{if } t = 1, \\ p_{t-1}^{(g)} + 1, & \text{if } \psi_t^{(g)} = 1, \\ p_{t-1}^{(g)}, & \text{if } \psi_t^{(g)} = 0. \end{cases} \quad (1)$$

This priority is used as the primary maximization objective for the RRM algorithm, enforcing continuous service and satisfaction of the QoE constraints, but it also affects the fleet trajectory learning through observations and reward definitions, as explained in Sec. IV.

C. Channel Model

The channel model follows the urban macro (UMa) channel described in the 3GPP TR 38.901 [37]. The adopted channel model differentiates between line-of-sight (LoS) and NLoS propagation regimes. This distinction is based on the LoS probability ρ_L , which is defined as a function of the distance between the GUE g and the BS (UABS or MBS). The path loss variation due to shadowing can be described through a log-normal distribution with zero mean and with a standard deviation σ_{LoS} and σ_{NLoS} for LoS and NLoS, respectively. Consequently, the received power and the SINR can be derived as:

$$P_{\text{rx}} = \frac{P_{\text{tx}} G_{\text{rx}} G_{\text{tx}}}{PL}, \quad \text{SINR} = \frac{P_{\text{rx}}}{P_{\text{noise}} + \sum_{i=1}^{N_{\text{int}}} P_{\text{rx},i}}, \quad (2)$$

where P_{tx} is the transmitted power, G_{tx} and G_{rx} are the transmitter and receiver antenna gains, PL is the path loss calculated following Table 7.4.1-1 and 7.4.2-1 in [37], P_{noise} the noise power, N_{int} denotes the number of interferers and $P_{\text{rx},i}$ is the received power from the i -th interferer. The achievable data rate depends on the SINR through the Shannon capacity formula.

For what concerns the modelling of the UABS beams, by defining $\phi^{(u)}$ as the field of view of the UABS on the vertical plane, and $\Phi^{(u)} = 2\pi(1 - \cos(\phi^{(u)}/2))$, the corresponding solid angle, then the solid angle of the single beam may be approximated as $\Phi_{\text{beam}}^{(u)} \approx \Phi^{(u)}/N_{\text{beam}}$. Finally, the receiving gain of UABS can be expressed as follow [38]:

$$G_{\text{beam}} = \frac{41000}{(\Phi_{\text{beam}}^{(u)} \frac{360}{2\pi})^2}. \quad (3)$$

For the sake of simplicity, it is assumed that the radiation pattern of the equivalent beam is ideal, with gain G_{beam} inside $\Phi_{\text{beam}}^{(u)}$ and 0 dB outside, i.e. GUEs that are not inside a beam are not considered connected to the UABS, thus this assumption provides a worst-case scenario for what concerns the drone and vehicles connectivity.

IV. PROBLEM FORMULATION

The stochastic nature of the service environment, characterized by unknown user positions within a service area $\omega \in \Omega$, dynamic channel variability, and the impact of the RRM, makes the user state evolution analytically complex. As a consequence, determining the optimal fleet-wide mission trajectory $\mathbf{P}_{0:T,\omega}$ with direct and closed-form optimization is extremely complicated. This problem can be framed as a

sequential decision-making problem under uncertainty, allowing the use of MADRL algorithms, supported by a CTDE framework, to solve it. This approach enables each UABS to act as an autonomous agent, executing a decentralized control policy that maps real-time observations to trajectory decisions. To enable efficient learning and coordination within the fleet, the policy is learned as one unique model, shared across the entire fleet, and updated centrally during training to ease the burden of computation.

To achieve this, agents must go through an extensive learning phase of trial-and-error exploration. However, the efficiency of this exploration process represents a critical bottleneck. Conventional exploration strategies often fail to navigate the vast joint state-action space, leading to prohibitively slow convergence. This limitation is particularly evident in environments characterized by heterogeneous scenarios, where the inability to generalize across diverse tasks makes naive exploration inefficient. To address this, we reduce the number of episodes required to reach target performance by employing a meta-advisor, which is trained over the full set of operational scenarios and aims at improving exploration strategies. Indeed, through the use of meta-exploration, the fleet can learn effective policies in significantly less time, enabling online and safe training for UABS networks in real-world applications.

A. Decentralized Partially Observable MDP

To address the fleet trajectory design problem, we model it as a decentralized partially observable MDP (DPOMDP) with elements $(\mathcal{S}, \mathcal{O}, \mathcal{A}, s_0, \mathcal{P}, \mathcal{R})$, which provides the mathematical framework for multi-agent sequential decision-making under uncertainty. We consider a set of UABS trajectory design problems exhibiting structural similarities. They are referred to as *tasks* τ_i , all belonging to the task set \mathcal{T} . Each task is uniquely defined by its operational scenario, $\tau_i = (\omega_i, \mathbf{P}_{0,i})$, representing a specific service area ω_i and fleet initial takeoff positions $\mathbf{P}_{0,i}$. While all tasks share the same global state space \mathcal{S} , observation space \mathcal{O} , and action space \mathcal{A} , each task τ_i constitutes a distinct instance of the DPOMDP. Specifically, every task is characterized by a unique initial state distribution s_{0,τ_i} , transition function \mathcal{P}_{τ_i} , and reward function \mathcal{R}_{τ_i} .

The interaction loop for a given generic task τ_i is as follows. At each time step t , the environment is in a global state $s_t \in \mathcal{S}$, which is not directly accessible to the agents. The initial state s_0 is determined by the task's takeoff positions \mathbf{P}_0 . Each UABS $u \in \mathcal{U}$ perceives a local and limited observation $o_t^{(u)} \in \mathcal{O}$. This observation is a vector $o_t^{(u)} = [x_t^{(u)}, y_t^{(u)}, t, \mathbf{P}_t, \mathbf{b}_t^{(u)}]$, where: (i) $x_t^{(u)}, y_t^{(u)}$ the current UABS's position; (ii) t the current mission time step; (iii) \mathbf{P}_t the position vector of all the UABSs in the fleet; and (iv) $\mathbf{b}_t^{(u)}$ is the *per-beam information* that is a vector of size N_{beam} whose elements $b_{i,t}$ corresponds to the sum of priorities $p_t^{(g)}$ for all GUEs g served by the i -th beam of UABS u at time t . Without loss of generality, the global state s_t can be regarded as the union of all agents' local observations.

Based on this local observation, each agent u selects a discrete movement action $a_t^{(u)}$ from the action space $\mathcal{A} =$

$[\leftarrow, \uparrow, \rightarrow, \downarrow, \nwarrow, \nearrow, \searrow, \emptyset]$. This set includes eight directions of movement and the hovering in place action \emptyset . The combination of all individual actions defines the global action a_t .

The joint action a_t applied to the global state s_t produces a state transition according to the task-specific dynamic and transition probability function \mathcal{P}_{τ_i} , defining the probability $\mathcal{P}_{\tau_i}(s, a) = P(s_{t+1}|s_t, a_t)$ to transition to a new state s_{t+1} .

As a result of this transition, all agents receive a shared and global reward $r_t = r_t^{(u)}$, $\forall u \in \mathcal{U}$ based on the task-specific reward function $\mathcal{R}_{\tau_i}(s, a, s')$. This reward is defined as:

$$r_t = r_t^{(u)} = \frac{\sum_{u \in \mathcal{U}} \sum_{g \in \mathcal{G}} \psi_t^{(g, u)} p_t^{(g)}}{|\mathcal{U}|} \quad (4)$$

which represents the average number of users served by the whole fleet weighted by their priority $p_t^{(g)}$ at time t . The reward function is computed based on the centralized RRM module, which is treated as an integral part of the environment dynamics. For a given fleet configuration, the RRM module determines association and scheduling (see Appendix A), defining which GUEs are served and the resulting reward. This service-based metric captures the inherent aerial-terrestrial coordination. Moreover, it is task-specific because each task τ_i defines a unique service area ω_i with specific GUEs and MBS distributions, so identical state-action pairs may yield different service outcomes $\psi_t^{(g)}$ depending on the operational context.

Finally, agents will perceive the new state s_{t+1} via their next local observation o_{t+1} , completing the interaction loop at time t .

The agents' behavior within a given task τ_i is governed by a decentralized, task-specific policy $\pi_i(a_t^{(u)}|o_t^{(u)})$, mapping local observations to a probability distribution over actions. For each task $\tau_i \in \mathcal{T}$, the objective is to learn an optimal policy π_i^* that maximizes the expected episodic cumulative discounted reward, that is:

$$\pi_i^* = \arg \max_{\pi_i} \mathbb{E}_{\pi_i, \mathcal{P}_{\tau_i}} \left[\sum_{t=0}^T \gamma^t r_t \right] \quad (5)$$

with $\gamma \in (0, 1)$ the discount factor, balancing the importance of immediate and future rewards. The expectation is taken over all possible state-action pairs generated by agents following their policy π_i in the task environment τ_i with transition functions \mathcal{P}_{τ_i} and reward function $\mathcal{R}_{\tau_i}(s, a, s')$. Since all agents receive a shared reward, optimizing this objective induces the collaborative fleet behavior. Thus, the optimal mission fleet trajectory $\mathbf{P}_{0:T, \omega_i}$ corresponds to the sequence of UABSs positions resulting from agents following policy π_i^* at each time step t .

B. Multi-Agent Deep Reinforcement Learning System

To find the optimal policy π_i^* and solve the problem defined by Eq. (5) for each task τ_i , we employ the double dueling deep Q-network (3DQN) algorithm. 3DQN is a state-of-the-art, off-policy deep reinforcement learning (DRL) algorithm that improves upon the vanilla deep Q-network (DQN) [39] by integrating the Double DQN principle [40] and the Dueling Network architecture [41]. The algorithm aims to learn the

optimal action-value function, $Q_i^*(o, a)$, for each task τ_i . This function, Q_{π_i} , for a given policy π_i , observation o_t , and action a_t is defined as the expected discounted return:

$$Q_{\pi_i}(o, a) = \mathbb{E}_{\pi_i} \left[\sum_{k=t}^{T-1} \gamma^{k-t} r_k \mid o = o_t, a = a_t \right] \quad (6)$$

This represents the expected cumulative reward achieved by taking action a_t in observation o_t and subsequently following policy π_i until the end of the episode.

For each task τ_i , 3DQN employs two neural networks: an *online* network with parameters θ_i and a *target* network with parameters θ_i^- . These networks receive a per-agent observation $o_t^{(u)}$ as input and output the estimated Q-value for each possible action $a \in \mathcal{A}$. The optimal actions $\bar{a}_t^{(u)}$ are then selected according to:

$$\bar{a}_t^{(u)} = \arg \max_a Q_{\pi_i}(o_t^{(u)}, a | \theta_i) \quad (7)$$

Furthermore, networks implement a dueling architecture, which decomposes the Q-value into a state-value $V(o)$ and a state-action advantage $A(o, a)$. The advantage represents the relative advantage of each action given the current observation, leading to improved learning performance.

To update the network parameters, all agents u operating on task τ_i collect experience tuples $(o_t^{(u)}, a_t^{(u)}, r_t, o_{t+1}^{(u)})$ at each time step t , storing them in a task-specific replay buffer \mathcal{K}_i . At each training iteration, a batch of $|k|$ experiences is randomly drawn from \mathcal{K}_i . We denote the e -th experience tuple in this batch as (o_e, a_e, r_e, o'_e) , where o'_e corresponds to the $o_{t+1}^{(u)}$ from the original tuple. The online parameters θ_i are updated via gradient descent:

$$\theta_i \leftarrow \theta_i - \alpha \nabla_{\theta_i} L(\theta_i) \quad (8)$$

where α is the learning rate and $L(\theta_i)$ is the mean-squared error loss, defined using the Double DQN target y_e :

$$L(\theta_i) = \frac{1}{|k|} \sum_{e=1}^{|k|} (y_e - Q(o_e, a_e | \theta_i))^2 \quad (9)$$

where $y_e = r_e + \gamma Q(o'_e, a' | \theta_i^-)$
 $a' = \arg \max_a Q(o'_e, a | \theta_i)$

This target y_e decouples the action selection, provided by the online network θ_i , from the value estimation, which uses the target network θ_i^- for its estimation, stabilizing learning. Every Y training iterations, the online network parameters are copied to the target network: $\theta_i^- \leftarrow \theta_i$.

This MADRL system is supported by the CTDE architecture shown in Fig. 2, which allows agents to train a model in a centralized manner, with agents performing inference of the learned model in a distributed way. Each UABS acts as a distributed agent, interacting continuously with the environment by performing actions based on local observations. Each experience tuple is then forwarded to the controller. The controller holds the shared replay buffer \mathcal{K}_i for each task, and it is in charge of training the learning models θ_i . The updated online parameters θ_i are then forwarded to each agent. This architecture enables system efficiency by reducing

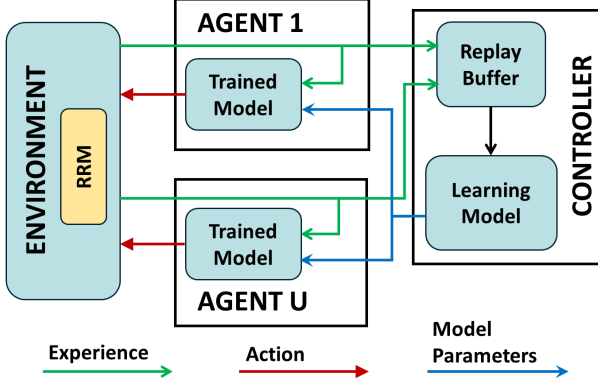


Fig. 2: CTDE architecture for UABS-aided vehicular networks. Each UABS $1, \dots, U$ has a shared local copy of the trained model, which is updated periodically by the controller entity from experiences gathered by all the autonomous agents.

the computational burden on each agent. It is assumed that the controller is co-located with the terrestrial MBS, ensuring that the exchange of experiences and models is performed leveraging the backhaul link used for user traffic. For the sake of simplicity, this overhead communication is not accounted for in the RRM procedure; however, its effect on the whole network performance was investigated in [42]. Leveraging this architecture, where the learning loop is embedded within the network infrastructure, our framework establishes a practical basis for an online training procedure. Here, online means that learning models are updated while the system is in execution, i.e., not relying on offline pre-training, leveraging the existing backhaul connectivity to exchange experiences and model updates. In this paper, we validate the proposed online learning architecture through simulations; nevertheless, the same CTDE loop can be executed over an operational network. Online training is particularly relevant in complex urban deployments, where the actual road traffic distribution, channel conditions, and interference patterns may differ significantly from those assumed in offline simulators, causing model mismatch [43]. However, deploying learning agents in a live network introduces a critical performance requirement: time-to-proficiency, i.e., how quickly agents converge to a useful policy without prolonged periods of poor service. To address this, we propose the MAMO system, which provides guided exploration and drastically reduces time-to-proficiency, making online multi-task adaptation quicker and safer.

V. EXPLORATION POLICIES

When dealing with MADRL algorithms, each agent must balance the exploration-exploitation tradeoff to train efficiently. Early in training, when policy parameters are affected by random initialization, exploration facilitates the collection of experiences $(o_t^{(u)}, a_t^{(u)}, r_t^{(u)}, o_{t+1}^{(u)})$, guiding model updates. However, inefficient or overly prolonged exploration can limit the exploitation of learned knowledge, leading to suboptimal convergence and longer training [23]. In contrast, an efficient exploration allows agents to characterize the task-specific dynamics, quickly maximizing the expected cumulative reward.

In this work, we compare two exploration strategies for the UABSS's fleet, a classical and a meta-learning driven approach.

A. ϵ -greedy

In this widely adopted baseline [44], each agent $u \in \mathcal{U}$ selects a random action with probability ϵ_i and with probability $1 - \epsilon_i$ chooses the exploitation action $\tilde{a}_t^{(u)}$ based on the current observation $o_t^{(u)}$, as defined in Eq.(7), according to the current policy parameters θ_i . Throughout a training of N episodes, ϵ_i is linearly decayed following:

$$\epsilon_i = \max \left(\epsilon_{i,\min}, 1 - \frac{(1 - \epsilon_{i,\min}) \cdot n}{\epsilon_{i,\text{frac}} \cdot N} \right) \quad (10)$$

with ϵ_{frac} representing the fraction of episodes over which the decay occurs, ϵ_{\min} the minimum exploration probability the agent will maintain after the decaying phase, and n the current episode. This exploration policy is a well-known approach, adopted widely in the literature due to its simplicity. However, it can lead to suboptimal performance or slower training time due to the complex tuning of the $\epsilon_{i,\text{frac}}$ hyperparameter. While other exploration alternatives exist, we focus on ϵ -greedy as a standard baseline to enabling more direct comparison with the proposed meta-advisor. Additionally, several alternatives rely on state visitation or confidence estimates whose applicability under partial observability and multi-agent non-stationarity can be limited, whereas ϵ -greedy remains simple and broadly applicable. A schematic representation of applying ϵ -greedy exploration to a generic set of tasks \mathcal{T} is shown in Fig. 3a

B. Multi-Agent Meta-Advisor

The random action selection of the ϵ -greedy approach can negatively affect navigation by causing unnecessary exploration that reduces learning efficiency. Moreover, it lacks mechanisms to exploit similarities among tasks τ_i to make the exploration phase more efficient. These limitations reduce the time-to-proficiency of the fleet, critical for the online learning system adopted. To overcome this, we introduce a context-aided deep multi-agent meta-advisor that guides the exploration phase using prior knowledge from the whole set of tasks \mathcal{T} . This advisor learns a shared exploration policy μ that provides exploration actions $\tilde{a}_t^{(u)}$ to agents based on an augmented observation $\tilde{o}_t^{(u)} = o_t^{(u)} \parallel \text{Id}(\omega_{\tau_i})$, with $o_t^{(u)}$ the original agent observation and $\text{Id}()$ a function mapping the service area ω_{τ_i} to a one-hot encoded vector. This additional context enhances the robustness of the advisor to heterogeneous service areas while maintaining generalization across all tasks in \mathcal{T} , as previously studied in our prior work [18]. Specifically, the advisor selects the exploration action $\tilde{a}_t^{(u)}$ by maximizing its action-value function:

$$\tilde{a}_t^{(u)} = \arg \max_a Q_\mu(\tilde{o}_t^{(u)}, a | \theta_\mu), \quad (11)$$

with θ_μ the parameters of the meta-advisor network.

The training of the advisor happens in parallel with the individual agents: while each agent learns its task-specific exploitation policy π_{τ_i} , the meta-advisor learns μ from the collective experiences obtained by agents in all the tasks and

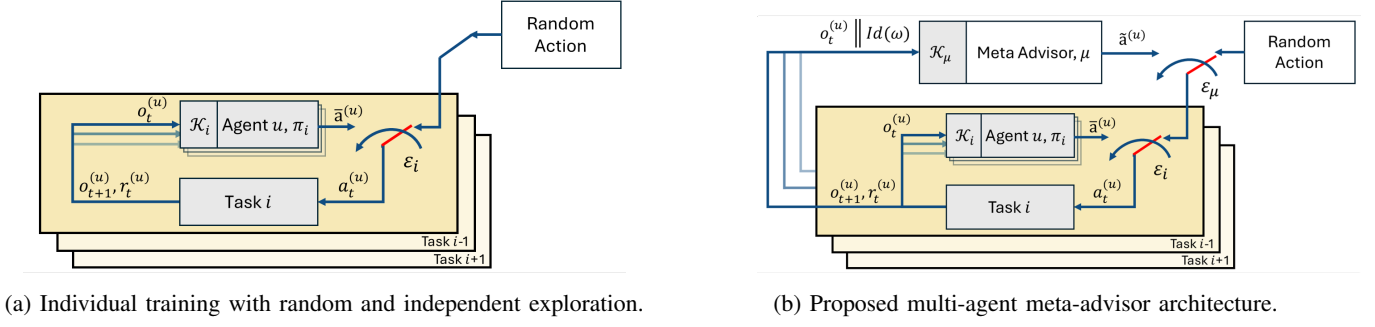


Fig. 3: Exploration strategies for multi task training.

stored in a shared replay buffer \mathcal{K}_μ . The existing core network supports the exchange of experiences among tasks, eliminating the need for additional wireless transmissions. Without loss of generality, the model is trained via the 3DQN algorithm with parameters θ_μ and θ_μ^- , and an ε_μ -greedy policy assuming $\varepsilon_{\mu,\text{frac}} << 1$ for its training. We adopt this value-based off-policy formulation to exploit experience replay and improve sample-efficiency of the advisor across tasks; policy-based meta-advisors are possible, but are left for future work. When the meta-advisor is employed as exploration policy, ε_i refers to the probability of selecting an exploration action for agent i for task τ_i , which can either random or selected by the meta-advisor depending on the value of ε_μ . It is highlighted that the advisor acts as an external module overseeing the parallel training of other agents, thus it can be trained with different hyperparameters or DRL algorithms. A representation of the meta-advisor architecture is reported in Fig. 3b.

C. Advisor Override

In our approach, the combination of a task-specific model, a meta-advisor, and a generic exploration policy provides each agent with three distinct types of candidate actions at each time step, namely:

- *exploit*, where the agent chooses the best action exploiting the current task-specific model learned, $\bar{a}_t^{(u)}$;
- *meta*, where the agent uses the action provided by the trained meta-advisor to perform safe and improved exploration, $\tilde{a}_t^{(u)}$;
- *random*, where the agent performs standard random exploration.

The process of choosing which of these three action types to execute is what we define as an agent specific *behavior selection*. To formalize this, we define the preliminary behavior selection variable $\tilde{\zeta}_t^{(u)}$:

$$\tilde{\zeta}_t^{(u)} = \begin{cases} \text{random} & \text{with prob. } \varepsilon_i \cdot \varepsilon_\mu \\ \text{meta} & \text{with prob. } \varepsilon_i \cdot (1 - \varepsilon_\mu) \\ \text{exploit} & \text{with prob. } (1 - \varepsilon_i) \end{cases} \quad (12)$$

This selection of behaviors is random and based on the current values of ε_i and ε_μ , which depend on the hyperparameters set at the beginning of training. However, the potential overconfidence of the meta-advisor in prescribing a specific meta exploration action \tilde{a} poses a risk of constraining

agents, particularly when encountering novel states within a given task. Furthermore, the original formulation may not fully account for the inherent non-stationarity of multi agent and multi task environments. In such settings, the shared advisor model may inherently bias its convergence towards a subset of simpler tasks, where rewards are more readily accessible, while failing to provide adequate guidance for more complex scenarios. This imbalance could lead to a biased advisor that disproportionately benefits certain agents or tasks at the expense of others. This can be more evident in the case of fleet operations, where each task requires discovering a specific cooperative trajectory. To this end, we introduce the concept of *advisor override*. This technique allows an agent with a preliminary mode meta at a given time step, i.e. $\tilde{\zeta}_t^{(u)} = \text{meta}$, to switch to random behavior mode if this condition is met:

$$\begin{aligned} \mathcal{C}_{t,\text{m} \rightarrow \text{r}}^{(u)} \triangleq & [\tilde{\zeta}_t^{(u)} = \text{meta}] \wedge \\ & \left(Q_{\pi_i} \left(o_t^{(u)}, \tilde{a}_t^{(u)} \mid \theta_i \right) < \frac{1}{|\mathcal{A}|} \sum_{a \in \mathcal{A}} Q_{\pi_i} \left(o_t^{(u)}, a \mid \theta_i \right) \right) \end{aligned} \quad (13)$$

where, $o_t^{(u)}$ is the current agent observation, $\tilde{a}_t^{(u)}$ is the action provided by the meta-advisor, and $Q_{\pi_i}(o_t^{(u)}, a \mid \theta_i)$ are the Q-value calculated for a generic action a and the current observation given the task-specific policy π_i . In other words, the advisor override is triggered whenever the task-specific model for task τ_i predicts that the action suggested by the meta-advisor yields a lower long-term reward, measured by its estimated Q-value, than the average reward expected from the other available actions. This mechanism has twofold advantages. On one hand, it allows the advisor to gather more heterogeneous experiences, avoiding overconfidence and overfitting in the early stage of training. On the other hand, it protects the exploitation model π_i from a biased meta-advisor, allowing it to perform standard exploration when necessary. It is important to notice that in the case of advisor rejection, the agent will perform standard random exploration considering the whole action space, with a non-zero probability of selecting the rejected action. This allows for ignoring the contribution of the advisor while minimizing the potential biases introduced by this mechanism. Advisor override draws inspiration from [29], however, it does not require a pre-training phase, making this technique feasible for online and parallel training among

Algorithm 1: MAMO online training

```

1: Initialize advisor network  $\theta_\mu$ , initialize task networks  $\theta_i, i = 1, \dots, |\mathcal{T}|$ 
2: for  $n = 0, \dots, N - 1$  do
3:   for  $\tau_i \in \mathcal{T}$  do
4:      $s_0 \leftarrow s_{0,\tau_i}$ 
5:     update  $\epsilon_i$  according to (10) with  $\epsilon_{\text{frac}} = \epsilon_{i,\text{frac}}$ 
6:     update  $\epsilon_\mu$  according to (10) with  $\epsilon_{\text{frac}} = \epsilon_{\mu,\text{frac}}$ 
7:     for  $t = 0, \dots, T - 1$  do
8:       for  $u \in \mathcal{U}$  do
9:          $\tilde{o}_t^{(u)} \leftarrow o_t^{(u)} \parallel \text{Id}(\omega_{\tau_i})$ 
10:         $\zeta_t^{(u)} \leftarrow \begin{cases} \text{random, with prb. } \epsilon_i \cdot \epsilon_\mu \\ \text{meta, with prb. } (1 - \epsilon_\mu) \cdot \epsilon_i \\ \text{exploit, otherwise} \end{cases}$ 
11:         $\zeta_t^{(u)} \leftarrow \begin{cases} \text{random, if adv. override is enabled} \\ \text{and } \mathcal{C}_{t,m \rightarrow r}^{(u)} \text{ holds} \\ \zeta_t^{(u)}, \text{ otherwise} \end{cases}$ 
12:         $a_t^{(u)} \leftarrow \begin{cases} \text{random, } \zeta_t^{(u)} = \text{random} \\ \arg \max_a Q_\mu(\tilde{o}_t^{(u)}, a), \zeta_t^{(u)} = \text{meta} \\ \arg \max_a Q_{\pi_i}(o_t^{(u)}, a), \zeta_t^{(u)} = \text{exploit} \end{cases}$ 
13:      end for
14:       $s_t \leftarrow \{o_t^{(u)}\}_{u \in \mathcal{U}}$ 
15:       $a_t \leftarrow \{a_t^{(u)}\}_{u \in \mathcal{U}}$ 
16:       $r_t \sim R_i(s_t, a_t)$ 
17:       $s_{t+1} \sim P_i(s_t, a_t)$ 
18:      for  $u \in \mathcal{U}$  do
19:         $\tilde{o}_{t+1}^{(u)} \leftarrow o^{(u)}_{t+1} \parallel \text{Id}(\omega_{\tau_i})$ 
20:         $\mathcal{K}_i \leftarrow \{o_t^{(u)}, a_t^{(u)}, r_t^{(u)}, o_{t+1}^{(u)}\}$ 
21:         $\mathcal{K}_\mu \leftarrow \{\tilde{o}_t^{(u)}, a_t^{(u)}, r_t^{(u)}, \tilde{o}_{t+1}^{(u)}\}$ 
22:      end for
23:      Train  $\theta_i$  with batch  $k \sim \mathcal{K}_i$  according to (9)
24:    end for
25:  end for
26:  for  $j = 0, \dots, J - 1$  do
27:    Train  $\theta_\mu$  with batch  $k \sim \mathcal{K}_\mu$  according to (9)
28:  end for
29: end for

```

multiple tasks. The final behavior mode is then derived as:

$$\zeta_t^{(u)} = \begin{cases} \text{random, if } \mathcal{C}_{t,m \rightarrow r}^{(u)} \text{ holds} \\ \zeta_t^{(u)}, \text{ otherwise.} \end{cases} \quad (14)$$

The overall MAMO algorithm is reported in Algorithm 1.

VI. NUMERICAL RESULTS

A. Simulation Settings

This section details the evaluation of the proposed MAMO exploration policy for multi-scenario fleet trajectory design. We consider a service area set $\Omega = \{\omega_1, \omega_2, \omega_3\}$, modeled after real districts in Bologna, Italy. These regions share the same dimensions $L \times W$, but differ in street layout map and in the number GUEs traversing the area. Within each area, a UABS fleet \mathcal{U} ($|\mathcal{U}| = 3$) is deployed to enhance GUE connectivity and service continuity in coordination with terrestrial MBSs. Fig. 4 illustrates the service areas, detailing the specific street layout map, and MBS position (depicted as a red triangle) for each. GUE mobility is simulated using simulation of urban mobility (SUMO) [45] to ensure realistic micro-mobility behavior under given road traffic distributions.

The whole task set \mathcal{T} consists of combinations of service areas and possible UABS fleet takeoff positions. Specifically, we define five possible takeoff settings: $\{[\xi_1, \xi_2, \xi_4], [\xi_1, \xi_3, \xi_4], [\xi_1, \xi_4, \xi_5], [\xi_2, \xi_3, \xi_5], [\xi_6, \xi_7, \xi_8]\}$, where $\xi_k = (x_k, y_k)$ represents predefined takeoff sites in each region. Tab. I summarizes the simulation parameters.

For each task, agents are trained for N episodes using the following learning strategies for comparison:

- **MAMO:** The proposed approach, where agents train a task-specific models θ_i exploiting the multi-agent meta advisor as an exploration policy, with advisor override enabled.
- **MAMA:** Agents train task-specific models θ_i using the multi-agent meta-advisor, but the advisor override mechanism is disabled, representing an ablation of the proposed solution.
- **ϵ -greedy:** Standard training using independent exploration between tasks, tested with varying decay rates $\epsilon_{i,\text{frac}}$.
- **Generalized:** A single model is trained for the entire task set \mathcal{T} . All agents share the same model for trajectory planning without per-task specialization.

For MAMO and MAMA, the meta-advisor model was trained in parallel with the task-specific models.

B. Performance Metrics

We evaluate performance based on the average return over a task set:

$$\bar{R}(n) = \frac{1}{|\mathcal{T}|} \sum_{\tau_i \in \mathcal{T}} R_{\tau_i,n} \quad (15)$$

where $R_{\tau_i,n} = \left(\sum_{u \in \mathcal{U}} \sum_{t=0}^T r_t^{(u)} \right)$ represents the total reward obtained by the fleet solving task τ_i at the n -th training episode. For clarity, results are smoothed using a moving average with a window length of 50.

To highlight the efficiency of the proposed meta-exploration approach, we quantify the time-to-proficiency concept via the *first successful episode (FSE)* metric, denoted by \hat{n}_{τ_i} . The FSE is the earliest episode in the training sequence of task τ_i where the return $R_{\tau_i,n}$ exceeds a success threshold R_{th} :

$$\hat{n}_{\tau_i} = \arg \min_n \{n \mid R_{\tau_i,n} \geq R_{\text{th}}\} \quad (16)$$

Reported values are averaged across multiple independent simulation runs for each approach.

We also track the episode *advisor override count (AOC)*, defined as:

$$\text{AOC}_{\tau_i}(n) = \sum_{t=0}^T \sum_{u \in \mathcal{U}} I_{\mathcal{C}_{t,m \rightarrow r}^{(u)}} \quad (17)$$

where $I_{\mathcal{C}_{t,m \rightarrow r}^{(u)}}$ is an indicator function equal to 1 when the override condition $\mathcal{C}_{t,m \rightarrow r}^{(u)}$ holds, and 0 otherwise. This metric quantifies how frequently the advisor override is triggered during episode n of task τ_i .

Finally, to assess the continuity of service provided by the UABS fleet, we report the *percentage of satisfied users* P_g , calculated as:

$$P_g = \frac{1}{|\mathcal{G}|} \sum_{g \in \mathcal{G}} \frac{N_g^{(\text{sat})}}{N_g} \quad (18)$$

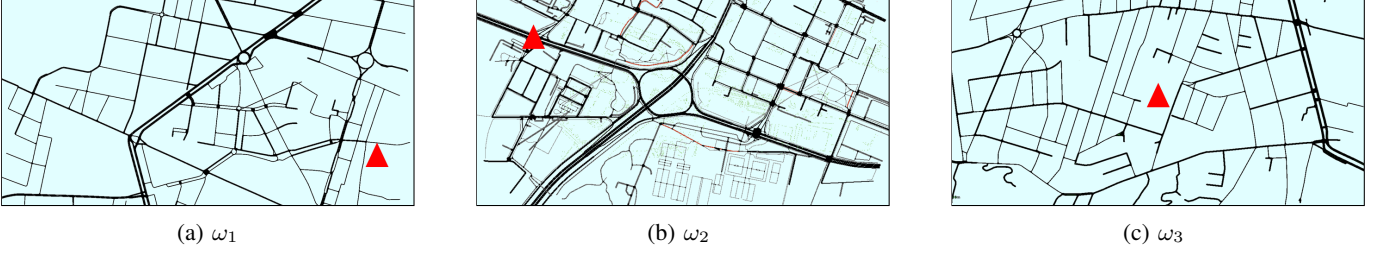


Fig. 4: Service area considered, with red triangles representing the MBS position.

$v^{(u)}$	20 m/s	$h^{(u)}$	100 m	ϕ	100°	ξ_1	(0, 0)
T	270 s	T_s	10 s	$ \mathcal{G} $ [$\omega_1, \omega_2, \omega_3$]	[200, 180, 90]	ξ_2	(L , 0)
f_c	30 GHz	B	9	P_{tx}	14 dBm	ξ_3	(0, W)
G_{tx}	0 dB	G_{rx}	23 dB	P_n	-106 dBm	ξ_4	(L , W)
$\epsilon_{\mu, \text{frac}}$	0.2	$\epsilon_{i, \text{frac}}$	0.6	ϵ_{\min}	0.05	ξ_5	($\frac{L}{2}$, $\frac{W}{2}$)
$ \mathcal{K}_i $	5e+4	$ \mathcal{K}_\mu $	1e+6	k	128	ξ_6	($\frac{L}{4}$, $\frac{3W}{4}$)
Y	100	γ	0.99	J	2700	ξ_7	($\frac{3L}{4}$, $\frac{W}{4}$)
D	1 MBit	L	1500 m	W	700 m	ξ_8	($\frac{3L}{4}$, $\frac{3W}{4}$)

TABLE I: Simulation parameters.

where N_g is the total number of service windows for the g -th GUE, and $N_g^{(\text{sat})}$ denotes the windows where the service constraint $N_s \geq \hat{N}_s$ is met.

C. Training Performance Analysis

Fig. 5 illustrates the cumulative return averaged over all tasks associated with a specific service area. Note that while the training process considers the entire task set \mathcal{T} concurrently, the results are grouped by service area for clearer analysis, as each region is characterized by a different number of users, leading to different reward magnitudes. The proposed MAMO exploration policy consistently outperforms the benchmarks, demonstrating superior convergence speed and higher final returns. This robustness is maintained across all service areas despite significant variations in reward scale and environmental layout. A critical observation arises from the comparison with MAMA in the service area ω_3 . Here, the MAMA approach, lacking the advisor override mechanism, suffers a significant performance degradation compared to MAMO. This suggests that in specific scenarios, the meta-advisor may provide guidance that is less effective for a given task due to overfitting toward other tasks. Without the ability to reject these suggestions via the override mechanism, agents may follow less effective advice, limiting the approach's generalization capabilities and exploration proficiency. Regarding the standard ϵ -greedy baselines, results highlight the trade-off inherent in hyperparameter tuning. A slow decay ($\epsilon_{\text{frac}} = 0.6$) delays convergence significantly. Conversely, a fast decay ($\epsilon_{\text{frac}} = 0.2$) accelerates initial learning but leads to premature convergence to sub-optimal policies and plateauing, as evident in ω_2 and ω_3 , where it fails to match the final performance of MAMO. Finally, the *Generalized* approach fails to converge to a viable policy, underscoring the necessity of task-specific models; thus, a single shared policy cannot capture the distinct fleet trajectory requirements of different urban environments.

While the performance trends in Fig. 5 highlight the superiority of MAMO, a more granular comparative analysis of the

TABLE II: Win Ratio of proposed MAMO vs benchmarks. Bold results represent the strongest competitor for the task considered.

Task		MAMA	ϵ -greedy 0.2	ϵ -greedy 0.6	Gen
ω_1					
$[\xi_1, \xi_2, \xi_4]$		41.3%	3.4%	45.6%	100.0%
$[\xi_1, \xi_3, \xi_4]$		73.6%	63.1%	81.6%	100.0%
$[\xi_1, \xi_4, \xi_5]$		95.6%	95.5%	97.0%	100.0%
$[\xi_2, \xi_3, \xi_5]$		61.2%	21.9%	98.9%	100.0%
$[\xi_6, \xi_7, \xi_8]$		89.8%	44.4%	99.9%	100.0%
ω_2					
$[\xi_1, \xi_2, \xi_4]$		73.7%	68.9%	79.8%	100.0%
$[\xi_1, \xi_3, \xi_4]$		67.8%	79.6%	85.0%	100.0%
$[\xi_1, \xi_4, \xi_5]$		92.6%	77.6%	87.9%	100.0%
$[\xi_2, \xi_3, \xi_5]$		59.7%	65.6%	90.4%	100.0%
$[\xi_6, \xi_7, \xi_8]$		49.4%	80.3%	95.8%	100.0%
ω_3					
$[\xi_1, \xi_2, \xi_4]$		56.0 %	85.8%	100.0%	100.0%
$[\xi_1, \xi_3, \xi_4]$		86.6%	83.7%	98.9%	100.0%
$[\xi_1, \xi_4, \xi_5]$		96.4%	68.9%	100.0%	100.0%
$[\xi_2, \xi_3, \xi_5]$		100.0%	94.4%	100.0%	100.0%
$[\xi_6, \xi_7, \xi_8]$		98.1%	68.3%	70.3%	100.0%
Average		76.1%	66.8%	88.7%	100.0%

return for each task τ_i is provided in Tab. II via the *Win-Ratio*. It represents the percentage of training episodes n , out of the total N , in which the return $R_{\tau_i, n}$ achieved by MAMO is higher than that obtained by the considered benchmark at the same training episode n . Therefore, this metric captures the dominance of MAMO throughout the entire learning phase, with lower values indicating a more challenging opponent. According to the results in Tab. II, MAMA and ϵ -greedy with $\epsilon_{\text{frac}} = 0.2$ appear as the most competitive on average. However, the leaderboard varies significantly across tasks, confirming that classical and naive advisor exploration approaches lack robustness against task variations, whereas MAMO maintains consistent superiority.

Fig. 6 analyzes the training efficiency by plotting the FSE.

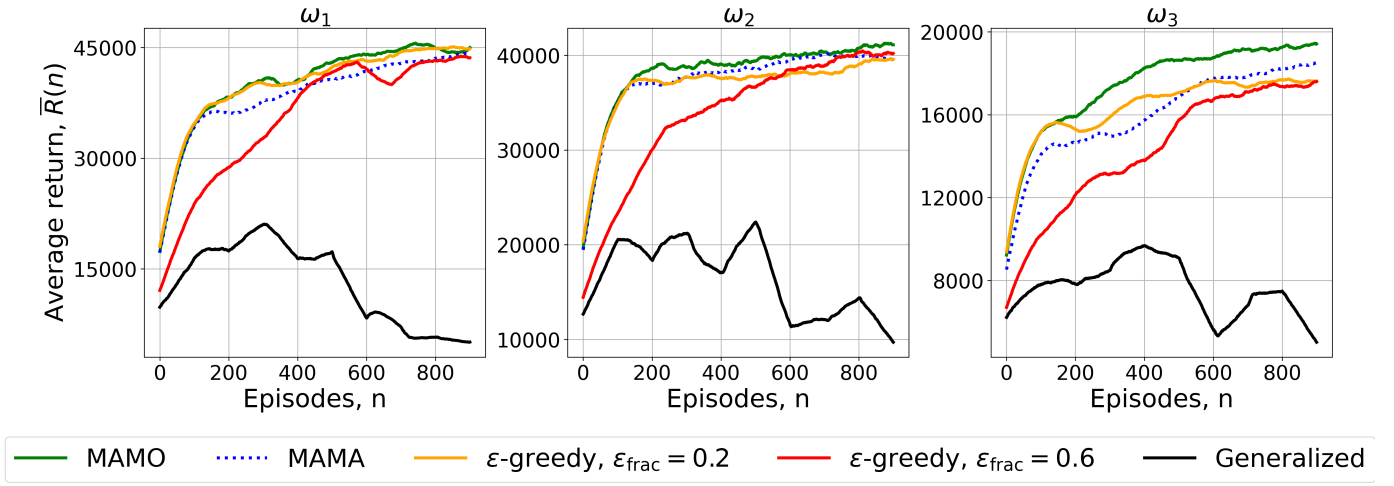


Fig. 5: Average return trends during training, averaged over tasks belonging to the same service area.

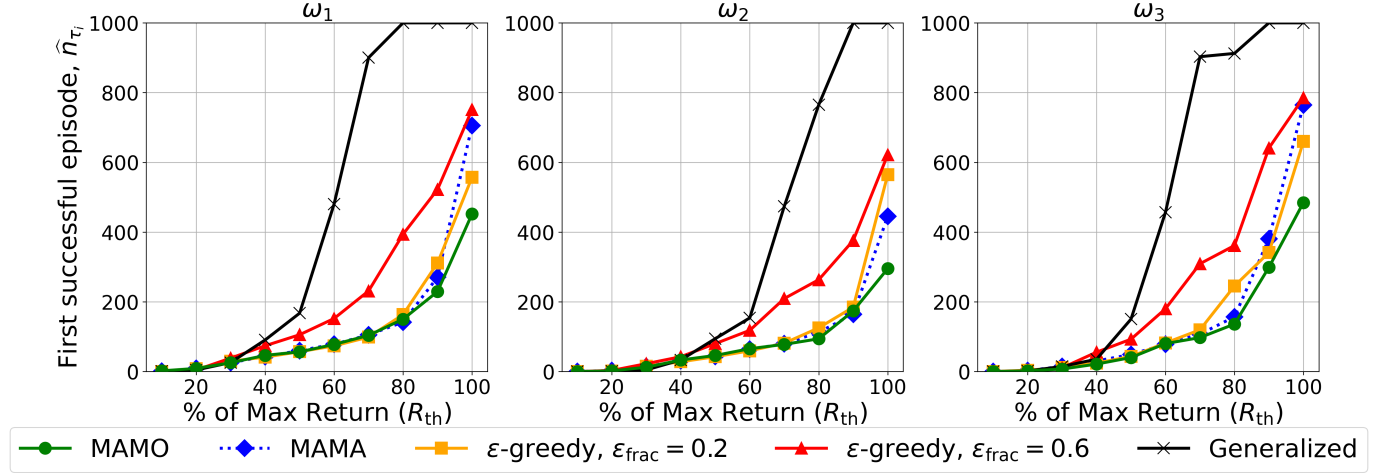


Fig. 6: First Successful Episode (\hat{n}_{τ_i}) as a function of the target return threshold, expressed as a percentage of the maximum return obtained during training. A lower curve indicates superior performance with the target reached in fewer episodes.

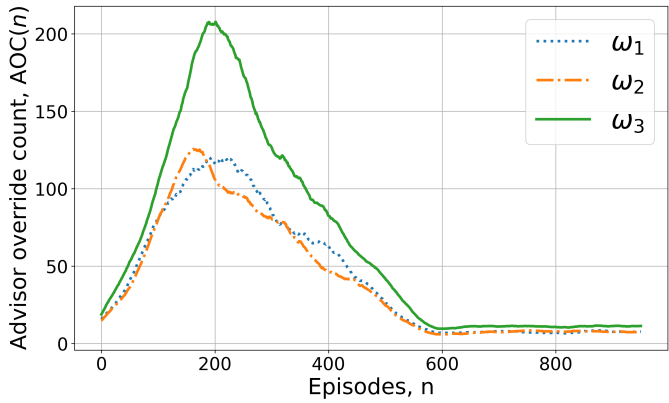


Fig. 7: Evolution of the Advisor Override Count (AOC) during training for different service areas.

We track the number of episodes required to reach a specific percentage of the achieved maximum return per task. For this metric, a curve with slower growth indicates that high-

performance thresholds are reached earlier in the training process. Across all areas, MAMO exhibits the flattest learning curves. In contrast, benchmark solutions, particularly Generalized and ε -greedy, show an asymptotic vertical rise near the 90%-100% return mark, indicating a struggle to refine the policy towards optimality within the 1000 training episodes. This capability to reach near-optimal returns in a fraction of the episodes is critical for online and safe learning systems, where reducing the “time-to-proficiency” directly translates to an immediate boost in network performance.

To explain the performance gap observed in Fig. 5, Fig. 7 details the AOC trends. The override frequency generally peaks between episodes 150 and 250, corresponding to the transition from random to meta-guided exploration. Most notably, the override count for service area ω_3 reaches a peak of ≈ 210 , nearly double the count observed for ω_1 and ω_2 . This high rejection rate indicates that the advisor is less reliable in the ω_3 scenario. This correlates perfectly with the failure of MAMA in Fig. 5. MAMA agents are forced to follow these task-mismatched suggestions, while MAMO

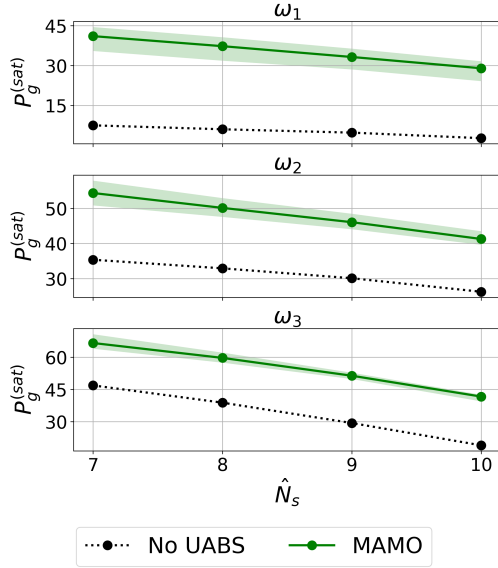


Fig. 8: Percentage of satisfied users (P_g) for the MAMO-trained fleet as a function of the service window threshold \hat{N}_s . The solid line represents the average across tasks, while the shaded area shows the minimum and maximum.

TABLE III: Traffic Load Distribution: MBS vs. Drone Fleet

Scenario	Total Load [Rx Packet]	MBS Load [%]	UABS A [%]	UABS B [%]	UABS C [%]
ω_1 MAMO	14332	25.7	23.5	22.4	28.4
	4236	100.0	-	-	-
ω_2 MAMO	19286	50.3	12.3	19.9	17.5
	11418	100.0	-	-	-
ω_3 MAMO	8974	49.2	14.1	16.6	20.1
	6316	100.0	-	-	-

agents trigger the protection mechanism, reverting to random exploration to avoid local optima.

D. Network Performance Analysis

In this section, we evaluate the learned adaptive trajectory model from a network performance perspective, focusing on agents trained via MAMO. Tab. III summarizes the network load distribution between the MBS and each UABS together with the total amount of received packets. These results represent averages across tasks within the same service area over episodes of duration T . These results indicate that the integration of the aerial segment significantly enhances overall network throughput even when the MBS and UABS fleet share the same system bandwidth. This improvement is most evident in service area ω_1 . Here the MBS, limited by its fixed location and NLoS dominated channel conditions, fails to meet GUEs uplink demand. In contrast, the deployment of the fleet increases the amount of received packets by more than 200%. Moreover, the load distribution among UABSs is balanced. This demonstrates the effective cooperative behavior that emerges within the fleet through the proposed MADRL learning framework.

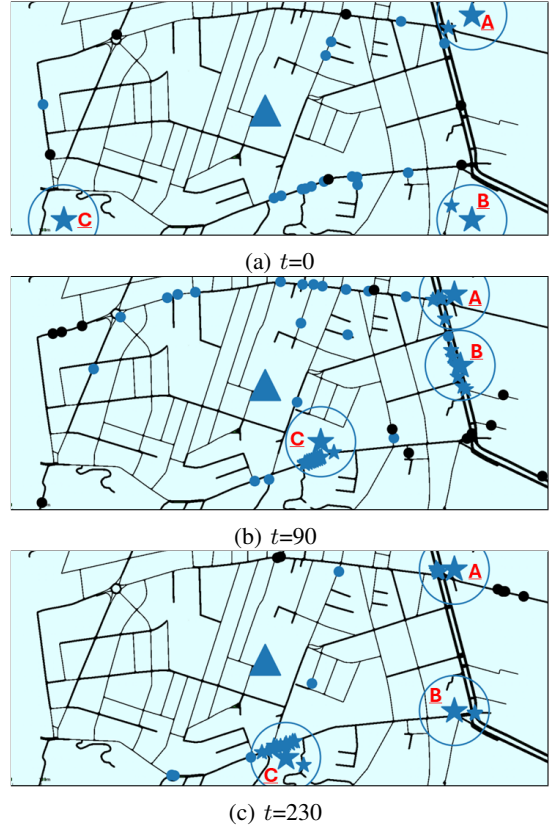


Fig. 9: Example of fleet trajectory learned by the UABSs. Star dots represent UABS, with circles their covered area. The triangle represents the MBS. (a) $t=0$, initial takeoff position (b) $t=90$ flight mission, UABS A serves users at the traffic light in upper-right corner, with UABS B close enough to ensure service continuity. UABS C focuses on users in the lower part of the service area (c) $t=230$, UABS B has moved to follow the available user, while UABS C changed its position to serve a greater amount of users.

Regarding the continuity of service, Fig. 8 reports the percentage of satisfied users, P_g , as a function of different service thresholds \hat{N}_s , averaged among tasks (solid line) and within the minimum and maximum reached in different tasks. Performance is heavily dependent on the specific task characteristics, as final network performance depends on both the UABS fleet trajectory design and the service provided by the MBS. Interestingly, despite being the most challenging for the advisor (as seen in the AOC analysis), service area ω_3 allows for the highest quality of service, with satisfied user rates reaching up to 70%. In contrast, ω_1 presents a stricter environment, capping at approximately 45%. In all scenarios, the MAMO-trained fleet maintains service continuity, although satisfaction naturally decreases as the service constraint \hat{N}_s increases. Finally, the contribution provided by the UABS fleet considerably improves the user QoE when compared to a scenario where only the MBS is present, as suggested by the gap between the solid and dotted curves.

Finally, Fig. 9 shows an example of the evolution of the fleet trajectory considering a generic task within service area ω_3 .

Throughout a flight mission, UABSs intelligently reposition themselves to provide continuity of service to GUEs.

VII. CONCLUSIONS

This work addressed the challenge of adaptive trajectory design for UABS fleets by developing an online MADRL framework that can generalize across diverse operational environments. The proposed MAMO framework introduces a meta-advisor that captures shared structural knowledge from multiple service areas and takeoff configurations. By combining this meta-advisor with a task-specific model, we enable agents to navigate the exploration-exploitation tradeoff effectively without the need for retraining when facing new scenarios. Moreover, a novel advisor rejection strategy allows agents to protect model training from potentially task-mismatched advisor suggestions. This strategy ensures both rapid multi-task adaptation and robustness to task heterogeneity.

Validation through simulations of realistic Bologna city districts confirms that MAMO provides superior adaptability compared to traditional methods. Specifically, our results show that MAMO reduces the first successful episode metric by up to 60% compared to ϵ -greedy baselines, while maintaining consistent performance across diverse tasks. The ablation study validates the necessity of the override mechanism, particularly in heterogeneous scenarios where the meta-advisor alone struggles to generalize. From a network performance perspective, the trained UABS fleet, cooperating with the existing MBS, provides substantial improvements in quality of service compared to the case where no drones are deployed. By facilitating coordinated and safe online learning, this approach offers a scalable solution for integrating autonomous aerial nodes into 6G vehicular networks.

APPENDIX

We consider radio resource units (RUs) spanning three dimensions: time, frequency, and space. In the frequency domain, the bandwidth is subdivided into subcarriers with a spacing of Δf . A RU consists of N_{sub} consecutive subcarriers, resulting in a total bandwidth of $B_{\text{RU}} = \Delta f \cdot N_{\text{sub}}$. In the time domain, transmission is divided into slots of duration T_{slot} . This duration depends on Δf , such that a single RU accommodates 14 orthogonal frequency-division multiplexing (OFDM) symbols.

Assuming the RRM algorithm executes with a periodicity of Δt , and given a total system bandwidth B_{sys} , the total number of RUs available for scheduling within one RRM period is:

$$W = \frac{B_{\text{sys}}}{B_{\text{RU}}} \cdot \frac{\Delta t}{T_{\text{slot}}}. \quad (19)$$

Furthermore, the spatial domain may provide orthogonality among resources, increasing capacity and mitigating interference. This spatial separation is implemented via beamforming at both the MBSs and UABSs, establishing directional links to the GUEs. Specifically, the UABS generates a fixed footprint on the ground composed of $N_{\text{beam}} = 9$ circular beams arranged in a 3×3 squared non-overlapping grid. As these beams are active simultaneously without overlap,

full frequency reuse is possible across beams. Conversely, MBS-GUE links are susceptible to building clutter and NLoS conditions; thus, perfect spatial separation is not guaranteed. Consequently, while MBS directional beams provide improved receiving gain, they do not support the full reuse architecture employed by the UABS.

The primary objective of the RRM algorithm is to maximize the number of served users, weighted by their priority to enforce service continuity. This is achieved by jointly optimizing user association (for both MBS and UABS fleets) and resource scheduling. To make this paper self-contained, the algorithm procedure is here briefly discussed; a more complete explanation can be found in [46]. The problem is formulated as a centralized, multi-UABS and multi-MBS integer linear program (ILP). At each time step t , the optimization runs on the following input variables: (i) k_{g,j_u} indicates whether vehicle g is covered by beam $j_u \in \mathcal{K}_u$ of UABS u , with \mathcal{K}_u the set of beams with cardinality N_{beam} ; (ii) $I_{g,m,u}$ and $I_{g,u,m}$ are binary variables capturing potential interference topology, for instance, $I_{g,m,u} = 1$ implies g is in range of both m and u , so a transmission from GUE g directed toward MBS m may interfere with UABS u . A similar implication holds when $I_{g,u,m} = 1$; (iii) $r_{g,u}, r_{g,m}, r_{u,m}$ and $r_{g,m,u}^I, r_{g,u,m}^I$ represents the per-RU rate achieved between transmitters and receivers in, respectively, absence or in presence of interference.

The ILP solution determines the network configuration through several decision variables: (i) $\lambda_{g,m}, \lambda_{g,u} \in \{0, 1\}$ represents user association, i.e. if GUE g is associated to MBS m or UABS u . Then, $\lambda_{u,m}$ controls the activation of the backhaul between UABS u and MBS m ; (ii) $w_{g,m}, w_{g,u} \in \{0, W\}$ are integer variables representing the number of RUs allocated to GUEs g for uplink transmission, while $w_{u,m} \in \{0, W\}$ the resources for backhaul; (iii) e_{j_u} , with $j_u \in \mathcal{K}_u$ are binary variables tracking the UABS beam activation. (iv) $\iota_{g,m,u}, \iota_{g,u,m}, \iota_{m,u}, \iota_{u,m} \in \{0, 1\}$ indicate the true interference relationship given a potential user association decision. For example, $\iota_{g,m,u} = 1$ if a transmission from g to m actually suffers interference from a simultaneous service at UABS u . As a result, the resource budget is computed assuming interference-limited rates. (v) ψ_g is the binary variable representing the successful upload of the packet sent by GUE g . Moreover, auxiliary variables $\psi_{g,u} = \psi_g \cdot \lambda_{g,u}$ and $\psi_{g,m} = \psi_g \cdot \lambda_{g,m}$ track the serving BS.

These variables are governed by the constraints (20b)–(20o). Constraints (20b) and (20c) ensure demand D_g is met by aggregating the rates of assigned RUs, accounting for both interference-free and interference-limited regimes, respectively. Resource limits are enforced by (20d) and (20e), which cap the RUs assigned by MBSs and UABSs, strictly accounting for backhaul overhead. Constraint (20f) enforces uplink transmission limits while guaranteeing sufficient backhaul capacity to support the aggregate vehicular traffic transmitted by each UABS. Constraints (20g) and (20h) restrict the active beams per UABS to N_{beam} , while constraints (20i)–(20k) ensure a vehicle connects to exactly one BS at a time. The logic linking potential interference to realized interference is enforced by (20l)–(20o). Specifically, the constraints (20l) and (20m) verify if there is at least one effective interferer

Algorithm 2: ILP formulation for the generalized RRM problem.

$$\mathcal{P} : \max \sum_{g \in \mathcal{G}} (\psi_g \cdot p_g) \quad (20a)$$

$$\text{s.t.: } \sum_{m \in \mathcal{M}} w_{g,m} r_{g,m} \Delta t + \sum_{u \in \mathcal{U}} \sum_{j_u \in \mathcal{K}_u} k_{g,j_u} w_{g,u} r_{g,u} \Delta t \geq \psi_g D_g, \forall g \in \mathcal{G} \quad (20b)$$

$$\sum_{m \in \mathcal{M}} w_{g,m} r_{g,m,u}^I \Delta t + \sum_{u \in \mathcal{U}} \sum_{j_u \in \mathcal{K}_u} k_{g,j_u} w_{g,u} r_{g,u,m}^I \Delta t \geq \left(\sum_{m \in \mathcal{M}} \iota_{g,m,u} + \sum_{u \in \mathcal{U}} \iota_{g,u,m} \right) D_g, \forall g \in \mathcal{G}, \forall u \in \mathcal{U}, \forall m \in \mathcal{M} \quad (20c)$$

$$\sum_{g \in \mathcal{G}} w_{g,m} + \sum_{u \in \mathcal{U}} w_{u,m} \leq W, \forall m \in \mathcal{M} \quad (20d)$$

$$\sum_{g \in \mathcal{G}} \sum_{j_u \in \mathcal{K}_u} w_{g,u} k_{g,j_u} r_{g,u} \leq \sum_{m \in \mathcal{M}} r_{u,m} w_{u,m}, \forall u \in \mathcal{U} \quad (20f)$$

$$\sum_{g \in \mathcal{G}} w_{g,u} k_{g,j_u} \leq e_{j_u} W, \forall u \in \mathcal{U}, \forall j_u \in \mathcal{K}_u \quad (20h)$$

$$w_{g,m} \leq \lambda_{g,m} W, \forall m \in \mathcal{M}, \forall g \in \mathcal{G} \quad (20j)$$

$$\iota_{m,u} \geq \sum_{g \in \mathcal{G}} \frac{I_{g,u,m} \lambda_{g,u}}{I_{g,u,m}}, \forall u \in \mathcal{U}, \forall m \in \mathcal{M} \quad (20l)$$

$$\iota_{g,m,u} \geq \lambda_{g,m} + \iota_{m,u} - 1, \forall g \in \mathcal{G}, \forall u \in \mathcal{U}, \forall m \in \mathcal{M} \quad (20n)$$

$$\sum_{g \in \mathcal{G}} k_{g,j_u} w_{g,u} + \sum_{m \in \mathcal{M}} w_{u,m} \leq W, \forall u \in \mathcal{U}, \forall j_u \in \mathcal{K}_u \quad (20e)$$

$$\sum_{j_u \in \mathcal{K}_u} e_{j_u} \leq N_{\text{beam}}, \forall u \in \mathcal{U} \quad (20g)$$

$$\sum_{m \in \mathcal{M}} \lambda_{g,m} + \sum_{u \in \mathcal{U}} \lambda_{g,u} \leq 1, \forall g \in \mathcal{G} \quad (20i)$$

$$w_{g,u} \leq \lambda_{g,u} W, \forall u \in \mathcal{U}, \forall g \in \mathcal{G} \quad (20k)$$

$$\iota_{u,m} \geq \sum_{g \in \mathcal{G}} \frac{I_{g,m,u} \lambda_{g,m}}{I_{g,m,u}}, \forall m \in \mathcal{M}, \forall u \in \mathcal{U} \quad (20m)$$

$$\iota_{g,u,m} \geq \lambda_{g,u} + \iota_{u,m} - 1, \forall g \in \mathcal{G}, \forall m \in \mathcal{M}, \forall u \in \mathcal{U} \quad (20o)$$

on the MBS that is connected to a UABSs u or vice versa, respectively. Then, (20n) determines if a UABS u interferes with an active link between g and m , while (20o) checks if an MBS m interferes with an active link between g and u .

ACKNOWLEDGMENT

This work has been carried out in the framework of the CNIT National Laboratory WiLab and the WiLab-Huawei Joint Innovation Center. We would like to thank Aman Jassal and Chan Zhou for the very fruitful discussion on this paper.

REFERENCES

- [1] G. Velez, A. Martin, G. Pastor, and E. Mutafungwa, “5g beyond 3gpp release 15 for connected automated mobility in cross-border contexts,” *Sensors*, vol. 20, no. 22, 2020. [Online]. Available: <https://www.mdpi.com/1424-8220/20/22/6622>
- [2] B. M. Masini, A. Bazzi, and A. Zanella, “A survey on the roadmap to mandate on board connectivity and enable V2V-based vehicular sensor networks,” *Sensors*, vol. 18, no. 7, 2018.
- [3] J. Choi, V. Va, N. Gonzalez-Prelcic, R. Daniels, C. R. Bhat, and R. W. Heath, “Millimeter-wave vehicular communication to support massive automotive sensing,” *IEEE Communications Magazine*, vol. 54, no. 12, pp. 160–167, 2016.
- [4] A. Bazzi, V. Todisco, A. Molinaro, A. O. Berthet, R. A. Stirling-Gallacher, and C. Campolo, “Exploiting repetitions and interference cancellation for the 6g-v2x sidelink autonomous mode,” *IEEE Transactions on Vehicular Technology*, pp. 1–15, 2025.
- [5] I. Sharya, M. Ergen, M. Hadri Azmi, S. Aldirmaz Çolak, R. Nordin, and Y. I. Daradkeh, “Key challenges, drivers and solutions for mobility management in 5g networks: A survey,” *IEEE Access*, vol. 8, pp. 172 534–172 552, 2020.
- [6] F. Bai and B. Krishnamachari, “Spatio-temporal variations of vehicle traffic in vanets: facts and implications,” in *Proceedings of the Sixth ACM International Workshop on VehiculAr InterNETworking*, ser. VANET ’09. New York, NY, USA: Association for Computing Machinery, 2009, p. 43–52. [Online]. Available: <https://doi.org/10.1145/1614269.1614278>
- [7] S. Schwarz and M. Rupp, “Society in motion: challenges for lte and beyond mobile communications,” *IEEE Communications Magazine*, vol. 54, no. 5, pp. 76–83, 2016.
- [8] M. Giordani, M. Rebato, A. Zanella, and M. Zorzi, “Coverage and connectivity analysis of millimeter wave vehicular networks,” *Ad Hoc Networks*, vol. 80, pp. 158–171, 2018. [Online]. Available: <https://www.sciencedirect.com/science/article/pii/S1570870518305687>
- [9] D. Saluja, R. Singh, N. Saluja, and S. Kumar, “Connectivity improvement of hybrid millimeter wave and microwave vehicular networks,” *IEEE Transactions on Intelligent Transportation Systems*, vol. 24, no. 2, pp. 1456–1464, 2023.
- [10] I. Ullah, H. El Sayed, S. Malik, and a. Manzoor Ahmed Khan, “Performance evaluation of quality of experience aware mobility management in heterogeneous cellular networks,” *IEEE Access*, vol. 12, pp. 97 994–98 003, 2024.
- [11] A. Giovannini, C. Campolo, V. Todisco, A. Molinaro, L. M. Amorosa, L. Lei, and A. Bazzi, “On the predictability of the best v2x path for infrastructure-assisted automated driving,” in *2025 IEEE Conference on Standards for Communications and Networking (CSCN)*, 2025, pp. 1–6.
- [12] N. Tafintsev, D. Moltchanov, M. Gerasimenko, M. Gapeyenko, J. Zhu, S.-p. Yeh, N. Himayat, S. Andreev, Y. Koucheryavy, and M. Valkama, “Aerial access and backhaul in mmwave b5g systems: Performance dynamics and optimization,” *IEEE Communications Magazine*, vol. 58, no. 2, pp. 93–99, 2020.
- [13] B. Galkin, J. Kibilda, and L. A. DaSilva, “A stochastic model for uav networks positioned above demand hotspots in urban environments,” *IEEE Transactions on Vehicular Technology*, vol. 68, no. 7, pp. 6985–6996, 2019.
- [14] L. Spampinato, D. Ferretti, C. Buratti, and R. Marini, “Joint Trajectory Design and Radio Resource Management for UAV-aided Vehicular Networks,” *IEEE Transactions on Vehicular Technology*, pp. 1–14, 2024.
- [15] D. Baldazo, J. Parras, and S. Zazo, “Decentralized multi-agent deep reinforcement learning in swarms of drones for flood monitoring,” in *2019 27th European Signal Processing Conference (EUSIPCO)*, 2019, pp. 1–5.
- [16] J. Li, B. Wan, and Z. Song, “Multi-agent deep reinforcement learning for group intelligence in emergency evacuation: A decentralized simulation-to-reality platform with perception-aware policies,” *Engineering Applications of Artificial Intelligence*, vol. 165, p. 113489, 2026. [Online]. Available: <https://www.sciencedirect.com/science/article/pii/S0952197625035201>
- [17] C. de Souza, R. Newbury, A. Cosgun, P. Castillo, B. Vidolov, and D. Kulic, “Decentralized multi-agent pursuit using deep reinforcement learning,” *IEEE Robotics and Automation Letters*, vol. 6, no. 3, pp. 4552–4559, 2021.
- [18] L. Spampinato, E. Testi, C. Buratti, and R. Marini, “Deep meta advisor-aided exploration for uav trajectory design in vehicular networks,” in *2025 IEEE International Conference on Acoustics, Speech, and Signal Processing Workshops (ICASSPW)*, 2025, pp. 1–5.
- [19] J. Hao, T. Yang, H. Tang, C. Bai, J. Liu, Z. Meng, P. Liu, and Z. Wang, “Exploration in deep reinforcement learning: From single-agent to multiagent domain,” *IEEE Transactions on Neural Networks and Learning Systems*, vol. 35, no. 7, pp. 8762–8782, 2024.
- [20] S. Govinda, B. Brik, and S. Harous, “A survey on deep reinforcement learning applications in autonomous systems: Applications, open

challenges, and future directions,” *IEEE Transactions on Intelligent Transportation Systems*, vol. 26, no. 7, pp. 11 088–11 113, 2025.

[21] F. Frattolillo, D. Brunori, and L. Iocchi, “Scalable and cooperative deep reinforcement learning approaches for multi-uav systems: A systematic review,” *Drones*, vol. 7, no. 4, 2023. [Online]. Available: <https://www.mdpi.com/2504-446X/7/4/236>

[22] W. Dabney, G. Ostrovski, and A. Barreto, “Temporally-extended ϵ -greedy exploration,” in *International Conference on Learning Representations*, 2021. [Online]. Available: <https://openreview.net/forum?id=ONBPHFZ7zG4>

[23] S. Zhang, H. Li, M. Wang, M. Liu, P.-Y. Chen, S. Lu, S. Liu, K. Murugesan, and S. Chaudhury, “On the convergence and sample complexity analysis of deep q-networks with \backslash epsilon-greedy exploration,” in *Advances in Neural Information Processing Systems*, A. Oh, T. Naumann, A. Globerson, K. Saenko, M. Hardt, and S. Levine, Eds., vol. 36. Curran Associates, Inc., 2023, pp. 13 064–13 102. [Online]. Available: https://proceedings.neurips.cc/paper_files/paper/2023/file/2a91de02871011d0090e662ffd6f2328-Paper-Conference.pdf

[24] S. Majumdar, R. Trivisonno, and G. Carle, “Understanding exploration and exploitation of q-learning agents in b5g network management,” in *2021 IEEE Globecom Workshops (GC Wkshps)*, 2021, pp. 1–6.

[25] S. Thadikamalla and P. Joshi, “Exploration strategies in adaptive traffic signal control: A comparative analysis of epsilon-greedy, ucb, softmax, and thomson sampling,” in *2023 7th International Symposium on Innovative Approaches in Smart Technologies (ISAS)*, 2023, pp. 1–8.

[26] J.-B. Kim, H.-B. Choi, and Y.-H. Han, “Strangeness-driven exploration in multi-agent reinforcement learning,” *Neural Networks*, vol. 172, p. 106149, 2024.

[27] C. Wang, T. Yu, and J. Liu, “Multi-agent curiosity via prediction error in local observations,” in *AAMAS*, 2022.

[28] F. M. Garcia and P. S. Thomas, “A Meta-MDP Approach to Exploration for Lifelong Reinforcement Learning,” *ArXiv*, vol. abs/1902.00843, 2019. [Online]. Available: <https://api.semanticscholar.org/CorpusID:59600091>

[29] S. Ganapathi Subramanian, M. E. Taylor, K. Larson, and M. Crowley, “Multi-agent advisor q-learning,” *JAIR*, vol. 74, pp. 1–74, 2022.

[30] H. Hu, B. Peng, Q. Zhang, Y. Peng, and J. Zhou, “Roma: Multi-agent reinforcement learning with emergent roles,” in *ICML*, 2021.

[31] A. Mahajan, T. Rashid, M. Samvelyan, and S. Whiteson, “Maven: Multi-agent variational exploration,” in *NeurIPS*, 2019.

[32] Y. Du, Y. Liu, Y. Li, B. Liu, and X. He, “Liir: Learning individual intrinsic reward in multi-agent reinforcement learning,” in *NeurIPS*, 2021.

[33] A. Gupta, S. Sharma *et al.*, “Contrastive representation learning for multi-agent reinforcement learning,” *arXiv preprint arXiv:2106.00643*, 2021.

[34] Y. Zheng, Y. Wu, K. Xu *et al.*, “Representation learning for exploration in multi-agent reinforcement learning,” in *ICLR*, 2022.

[35] K. Ganesan, P. B. Mallick, J. Löhr, D. Karampatsis, and A. Kunz, “5g v2x architecture and radio aspects,” in *2019 IEEE Conference on Standards for Communications and Networking (CSCN)*. IEEE, 2019, pp. 1–6.

[36] 5GAA, “C-V2X Use Cases Volume II: Examples and Service Level Requirements,” *White Paper*, Jun. 2019.

[37] 3GPP, “Technical Specification Group Radio Access Network; Study on channel model for frequencies from 0.5 to 100 GHz,” *3GPP TR 38.901 version 16.1.0*, Dec. 2019.

[38] V. K. Salvia, *Antenna and wave propagation*. Laxmi, 2007.

[39] V. Mnih, K. Kavukcuoglu, D. Silver, A. A. Rusu, J. Veness, M. G. Bellemare, A. Graves, M. A. Riedmiller, A. Fidjeland, G. Ostrovski, S. Petersen, C. Beattie, A. Sadik, I. Antonoglou, H. King, D. Kumaran, D. Wierstra, S. Legg, and D. Hassabis, “Human-level control through deep reinforcement learning,” *Nature*, vol. 518, pp. 529–533, 2015.

[40] H. v. Hasselt, A. Guez, and D. Silver, “Deep Reinforcement Learning with Double Q-Learning,” in *Proceedings of the Thirtieth AAAI Conference on Artificial Intelligence*, ser. AAAI’16. AAAI Press, 2016, p. 2094–2100.

[41] Z. Wang, T. Schaul, M. Hessel, H. Van Hasselt, M. Lanctot, and N. De Freitas, “Dueling Network Architectures for Deep Reinforcement Learning,” in *Proceedings of the 33rd International Conference on International Conference on Machine Learning - Volume 48*, ser. ICML’16. JMLR.org, 2016, p. 1995–2003.

[42] D. Ferretti, L. Spampinato, E. Testi, C. Buratti, and R. Marini, “Adaptive communication for joint trajectory and rrm in madrl-based uav networks,” in *2025 21th International Conference on Wireless and Mobile Computing, Networking and Communications (WiMob)*, 2025, pp. 1–6.

[43] E. Salvato, G. Fenu, E. Medvet, and F. A. Pellegrino, “Crossing the reality gap: A survey on sim-to-real transferability of robot controllers in reinforcement learning,” *IEEE Access*, vol. 9, pp. 153 171–153 187, 2021.

[44] R. S. Sutton and A. G. Barto, “Reinforcement learning: An introduction,” *MIT Press*, 2018.

[45] P. A. Lopez *et al.*, “Microscopic Traffic Simulation using SUMO,” in *Proc. ITSC*, Maui, USA, Nov. 2018, pp. 2575–2582.

[46] D. Ferretti, S. Mignardi, R. Marini, R. Verdone, and C. Buratti, “Qoe and cost-aware resource and interference management in aerial-terrestrial networks for vehicular applications,” *IEEE Transactions on Vehicular Technology*, pp. 1–12, 2024.